

Nanoscale

Accepted Manuscript



This is an *Accepted Manuscript*, which has been through the Royal Society of Chemistry peer review process and has been accepted for publication.

Accepted Manuscripts are published online shortly after acceptance, before technical editing, formatting and proof reading. Using this free service, authors can make their results available to the community, in citable form, before we publish the edited article. We will replace this *Accepted Manuscript* with the edited and formatted *Advance Article* as soon as it is available.

You can find more information about *Accepted Manuscripts* in the [Information for Authors](#).

Please note that technical editing may introduce minor changes to the text and/or graphics, which may alter content. The journal's standard [Terms & Conditions](#) and the [Ethical guidelines](#) still apply. In no event shall the Royal Society of Chemistry be held responsible for any errors or omissions in this *Accepted Manuscript* or any consequences arising from the use of any information it contains.

Cite this: DOI: 10.1039/c0xx00000x

www.rsc.org/xxxxxx

ARTICLE TYPE

Fabrication of SnO-SnO₂ nanocomposites with p-n heterojunctions for low-temperature sensing of NO₂ gas

Lei Li,^{a,b} Chunmei Zhang,^{a,c} and Wei Chen^{*a}

Received (in XXX, XXX) Xth XXXXXXXXX 20XX, Accepted Xth XXXXXXXXX 20XX

DOI: 10.1039/b000000x

In this report, the fabrication of novel SnO₂-SnO nanostructure with p-n heterojunction is achieved through a facile one-pot and low-cost hydrothermal process. The structure and properties of the nanocomposites were analyzed with X-ray techniques and electron microscopy. The HRTEM characterizations showed that p-n heterojunction was formed with small n-type SnO₂ nanocrystals dispersed on the surface of large p-type SnO crystals. Compared to the single SnO₂-based material, the gas sensor fabricated from SnO₂-SnO composite exhibited enhanced sensing performance for NO₂ gas detection with a limit of detection and sensitivity of 0.1 ppm and 0.26 ppm⁻¹, respectively, at relative low operation temperature (50 °C). Moreover, the p-n heterojunction exhibited high sensing selectivity for NO₂. Such high sensing sensitivity and low operation temperature make the SnO₂-SnO p-n nanomaterial promising gas sensor for practical NO₂ gas detection. The improved sensing response characteristics of the hybrid material could be attributed to the p-n junctions formed through the *in situ* growth of SnO₂ nanocrystals on SnO nanoplates. The present study is helpful for the design of novel gas sensing materials and the development of NO₂ gas sensors.

1. Introduction

Tin dioxide (SnO₂) nanomaterials have been widely applied in the field of gas sensing for decades due to its unique sensing properties, such as high sensitivity, fast response and high stability etc.^{1, 2} Tin dioxide is a typical n-type semiconductor material with rutile crystalline structure and wide band gap (3.6 eV). Many endeavors have been devoted to the design of SnO₂ nanostructures and have received many excellent achievements.^{1, 2} Especially, owing to its excellent tunable physicochemical properties and the size-, shape- and exposed surface-dependent gas sensing properties, SnO₂ nanomaterials with various structures have been designed for gas sensing, such as zero-dimensional (0D) particles^{3, 4} or clusters,⁵ one-dimensional (1D) nanofibers^{6, 7} or nanorods,^{8, 9} two-dimensional (2D) nanosheets¹⁰ and three-dimensional (3D) hierarchical and porous hollow structures,¹¹⁻¹⁴ etc. In order to overcome the intrinsic shortcomings of pure SnO₂ nanomaterials and to improve the sensing performance, large amount of SnO₂ nanomaterials doped with different dopants have been proposed recently. Among the doped materials, the semiconductor materials doped or loaded with noble metals such as Pt,¹⁵⁻¹⁸ Pd,¹⁹⁻²² Au,²³⁻²⁵ and Ag,^{26, 27} have been synthesized and the doped SnO₂ materials exhibited enhanced sensing performance. However, due to the high cost and the easy poisoning of noble metals by toxic gases,^{22, 28, 29} the application of noble metal-doped SnO₂ nanomaterials in gas

sensors are largely limited. In recent years, it was found that hybrid sensing materials fabricated from different types of semiconductors by forming p-n heterojunction with SnO₂ nanomaterials can effectively increase charge transfer and enhance the sensing properties.³⁰⁻³³

The unique heterojunction structure fabricated from SnO₂ and other doped or supported metal oxide materials with various morphologies exhibited outstanding gas sensing properties. Compared with gas sensors based on single SnO₂ material, the nano-gas-sensors fabricated from p-n heterojunction structure of SnO₂/metal oxides can largely overcome the shortcomings of high resistance, high working temperature and long response time, etc.^{30, 33} In a p-n junction structure, between the contact sections of n- and p-type semiconductor materials, the conduction and valence bands usually bend and the Fermi levels are equalized associated with the formation of depletion layers, which directly results in the improvement of the conductivity and the acceleration of response and recovery times.^{34, 35} Moreover, the morphologies of metal oxides with hierarchical structures can be tuned to enhance gas diffusion rate and enlarge the specific surface area, and thus to further improve the gas sensing properties. In recent years, the typical SnO₂-based nanomaterials with p-n heterojunction have been designed as gas sensors, for example SnO₂ nanoparticles-doped WO₃ nanolamella for NO₂ sensing,³⁶ α-Fe₂O₃ nanorods grown epitaxially on the surface of SnO₂ nanosheets for acetone sensing,³⁷ heterostructured CuO nanoparticles and SnO₂ nanowires for H₂S detection,³⁴ ZnO/SnO₂

core-shell structural microspheres for ethanol sensing³⁸ and so on. Meanwhile, the heterostructures of SnO₂ metal oxides materials are not only confined in gas sensing application, but also applied to electrochemical sensing,³⁹ photocatalysts,⁴⁰ lithium ion battery,⁴¹ dye-sensitized solar cells,⁴² etc.

Nitrogen dioxide (NO₂) is a kind of reddish brown, high activity gaseous substance, which is mainly released from high-temperature combustion processes, such as the emissions of exhaust gas of automobiles, exhaust gas discharged from power station and so on.^{43,44} It is deserved to mention that NO₂ is also a key composition of acid rain which will cause a variety of environmental effects, including the visibility reduction of atmosphere, surface water acidification and increased harmful toxins in fish and other aquatic organisms in water. Therefore, efficient sensing materials for sensitive detection of NO₂ gas in the ambient with fast response are essentially required.⁴⁵ In this paper, to develop practically useful NO₂ sensing materials, SnO-SnO₂ hybrids with p-n junction were fabricated through a one-step hydrothermal process. To the best of our knowledge, there is no report previously on the synthesis and NO₂ gas sensing properties of SnO-SnO₂ hybrid materials with p-n junction. The prepared SnO nanoplate-SnO₂ nanoparticle composites can effectively enhance the electrons transfer and improve the response to the target NO₂ gas. The gas sensing tests showed that detection of NO₂ with a limit of detection of 0.1 ppm can be realized at low temperature (50 °C) by using the prepared SnO-SnO₂ p-n junctions as sensing probes. The present study demonstrates that designing novel semiconductor-semiconductor nanostructures with p-n heterojunction is an efficient route to develop the next-generation gas sensors with improved sensing performance.

2. Experimental Section

2.1 Material preparation

All reagents are analytical grade and were used without further purification unless that was specified. The SnO-SnO₂ nanocomposites were synthesized by a hydrothermal process. Typically, 0.066 g of SnCl₂·2H₂O (Beijing Chemical Reagent Co., Ltd., China, AR, 98%) and 0.054 g of urea were dissolved in 15 mL of deionized water under moderate stirring for about 30 min until the mixture appear homogeneous milky solution. Then, the mixed solution was transferred to a 25 mL Teflon-lined stainless steel vessel and the hydrothermal process was performed at 180 °C for 16 h. The formed SnO₂-SnO composites were washed with water and ethanol by centrifugation (3000 rpm), and then dried at 40 °C for several hours in air to obtain the final product. In order to compare the gas sensing performances of the prepared SnO₂-SnO nanocomposites and single SnO₂ material, SnO₂ nanoparticles were also prepared by the same synthetic method and treatment procedure. In a typical synthesis, 0.105 g of SnCl₄·5H₂O (Chengdu Gracia Chemical Technology Co., Ltd., China, AR, 99%), 0.054 g of urea were dispersed in 15 mL deionized water under magnetic stirring. Notably, this mixed solution is colorless and clear, which is different from that of SnCl₂·2H₂O. The following hydrothermal and purification processes are same with the aforementioned.

2.2 Material characterization

The composition and crystalline structures of the products were characterized by X-ray powder diffraction (XRD) on a Bruker D8 Avance X-ray diffractometer between 10° and 90° using a Cu K α radiation source ($\lambda = 1.54 \text{ \AA}$). The morphologies and selected area electron diffraction of the composites were characterized by transmission electron microscope (TEM, JEOL 2000) and high resolution TEM (HRTEM, JEM-2010(HR) microscope). At the same time, the chemical states of the products were examined by X-ray photoelectron spectroscopy (XPS, VG Thermo ESCALAB 250 spectrometer). The Braunauer-Emmett-Teller (BET, Quantachrome Autosorb Automated Gas Sorption System) specific surface area and porosity properties analysis were also performed. UV-vis spectra were collected on a UV-3000PC Spectrophotometer (Shanghai Mapada Instruments Co., Ltd.). At last, the gas sensing properties of the materials were tested by a CGS-ITP (Chemical Gas Sensor-1 Temperature Pressure) intelligent gas sensing analysis system (Beijing Elite Tech Co., Ltd, China).

2.3 Gas sensing measurements

The gas sensing behaviors of the samples were tested on a heating ceramic plate of the CGS-ITP instrument by pressing sample firmly with two probes. The products were firstly mixed with N, N- dimethylformamide (DMF) to form homogeneous suspensions which were then drip-dropped on commercial ceramic substrates with Ag-Pd interdigitated electrodes. The as-prepared samples were dried at 55 °C during the process of drip-dropping in air. The gas sensing measurements were conducted with the prepared sensors at different operation temperatures with a fixed working voltage of 9 V. The operation temperature was changed by external temperature controller under heating ceramic plate and that could be adjusted from room temperature to 500 °C with the rate of 3-5 °C/s (relative humidity is about 38%). The sensor was preheated for about 30 min at certain target temperature until the resistance of the materials reached a stable range, and then was sealed in an 18 L test chamber. The target gas was injected into the test chamber through the injection pore. During the measurements, the fans for gas mixing were turned on till the resistance of material reaches a stable range. After gas sensing tests, the test chamber was opened to make the sensor expose to the fresh air and the fans were turned off. These procedures were repeated for the gas sensing tests at different conditions. Here, the response of the sensor is defined as $R = R_g/R_a$, where R_g and R_a are the resistances of sensor in target gas and air, respectively. The concentration of target gas could be calculated by equation 1:⁴³

$$(1) \quad Q = V \times C \times 10^{-6} \times \frac{273 + T_R}{273 + T_B}$$

Where Q is the volume of target gas, V is the volume of test chamber, C is the concentration of target gas, T_B is the operation temperature and T_R is the room temperature.

3. Results and Discussion

3.1 Synthesis and characterization of the gas sensing materials

In this study, two kinds of NO₂ gas sensing materials (SnO₂-SnO nanocomposites and single SnO₂ nanoparticles) were prepared by

one-pot hydrothermal processes. In the hydrothermal process,

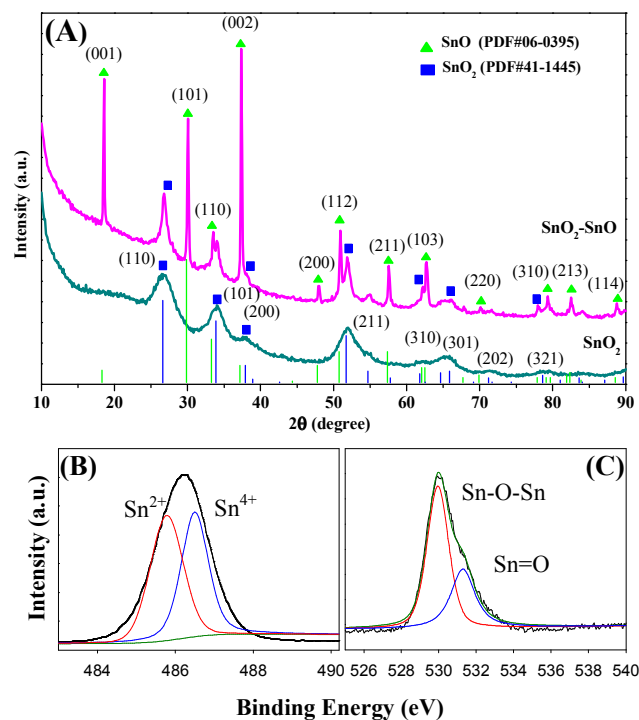


Fig. 1 (A) Typical XRD patterns of SnO₂-SnO nanocomposite and SnO₂ nanoparticles. For comparison, XRD data of bulk SnO (green bars) and SnO₂ (blue bars) from the joint Committee Powder Diffraction Standard are also included. High resolution XPS spectra of Sn 3d_{5/2} (B) and O1s (C) of the SnO₂-SnO nanocomposite.

urea plays a key role for the formation of SnO₂-SnO composite. When temperature is higher than 90 °C, urea begins to hydrolyze and NH₄⁺ and CO₃²⁻ will be slowly released. With temperature further increasing, CO₂ and OH⁻ can be produced from CO₃²⁻ and NH₄⁺, respectively.⁴⁶ Owing to the limited oxygen in the solution, only a small part of SnO can be converted to SnO₂ to form the SnO₂-SnO composite. While the totally oxygen-free condition is hard to achieve in the hydrothermal process, pure SnO product can not be prepared with the present method. The main reactions from Sn²⁺ and Sn⁴⁺ precursors could be described as follows.



The composition and crystalline structure of the obtained products were first characterized by X-ray techniques and electron microscopy. As shown in Fig. 1A, the XRD pattern of the heterojunction structured SnO₂-SnO composites agrees well with the standard cassiterite (SnO₂, JCPDS card no.41-1445) and romarchite (SnO, JCPDS card no.06-0395). However, the product synthesized from SnCl₄·5H₂O shows only cassiterite SnO₂ phase (JCPDS card no.41-1445). It is noteworthy that compared with the diffraction peaks of the pure SnO₂ sample, the intensity and full widths at half maximum (FWHM) of the diffraction peaks from the SnO₂-SnO composites are much stronger and narrower. These results imply that the SnO₂ nanocrystals formed in the

35 SnO₂-SnO composites have higher degree of crystallinity and

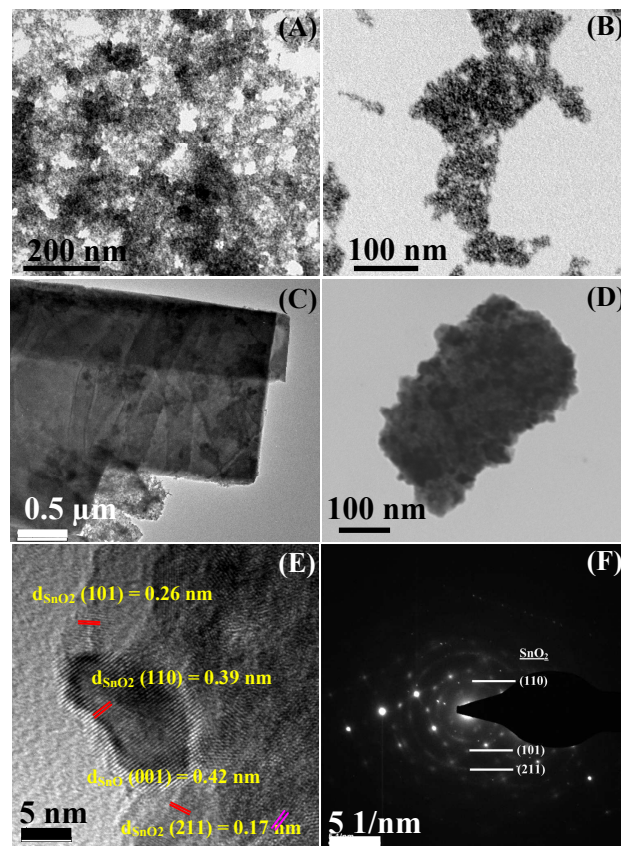


Fig. 2 (A, B) TEM images of the SnO₂ nanoparticles at different magnifications. (C, D) TEM images of the SnO₂-SnO hybrid at different magnifications. High-resolution TEM image (E) and the selected-area electron diffraction (SAED) pattern (F) of the SnO₂-SnO.

relatively larger crystal size than the pure SnO₂ sample. On the other hand, such results suggest that during the formation of SnO₂-SnO hybrid materials, the nucleation and crystal growth can be promoted. Interestingly, in the XRD pattern of the SnO₂-SnO, the intensity and FWHM of diffraction peaks from SnO are much stronger and narrower than those from the SnO₂ component, suggesting that the SnO nanocrystals are much larger than SnO₂ nanoparticles. Meanwhile, from the standard XRD data of SnO (JCPDS card no.06-0395), the diffraction peak of (101) has the highest intensity ($I_{(001)}/I_{(101)} = 0.1$, $I_{(002)}/I_{(101)} = 0.14$). However, in the XRD pattern of SnO₂-SnO composite, the diffraction peaks from (001) and (002) are much stronger than that of (101) with the much increased $I_{(001)}/I_{(101)}$, $I_{(002)}/I_{(101)}$ ratios of 1.1 and 1.26. Such XRD features strongly suggest that the formed SnO nanocrystals in SnO₂-SnO are predominated by exposed (001) facet. The lattice parameters of the (001), (101) and (002) facets were calculated to be $c = 0.485$, 0.485 and 0.436 nm, respectively, based on the MDI Jade 5.0 software. The crystallite sizes of SnO, SnO₂ in the SnO₂-SnO composite, and of the pure SnO₂ nanoparticles were evaluated to be 80.64, 28.4 and 4 nm, respectively, by the Scherrer equation: $d = 0.9\lambda/B_{2\theta} \cos\theta$ (λ : wavelength of the X-ray; θ : angle of the peak; $B_{2\theta}$: the peak width at half height) with the values of FWHM of the major

diffraction peaks of SnO (002) plane and SnO₂(110) planes. The calculated crystalline sizes are in accordance with the following results from TEM and HRTEM measurements.

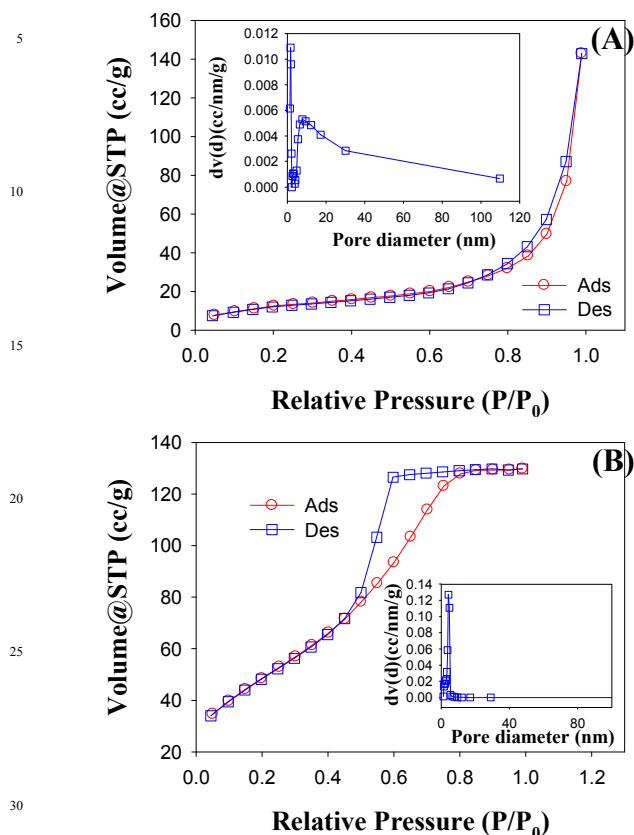


Fig. 3 N₂ adsorption–desorption isotherms of the SnO₂-SnO composite (A) and pure SnO₂ nanoparticles (B). Insets are the corresponding pore size distributions.

The XPS spectral measurements were also carried out to identify the chemical states of the SnO₂-SnO composite. Fig. S1 shows the full scale survey spectrum of the sample. Clearly, the peaks from Sn, O and C can be observed without the presence of any other impurities. From the high-resolution Sn 3d_{5/2} spectrum of the SnO₂-SnO composite shown in Fig. 1B, the two fitted peaks at 485.8 and 486.5 eV correspond to the Sn²⁺ and Sn⁴⁺ states, respectively.^{30, 47} Fig. 1C shows the high-resolution O 1s spectrum of the hybrid, in which the deconvoluted two peaks at binding energies of 529.9 and 531.2 eV correspond to the SnO₂ (Sn-O-Sn) and the oxygen of SnO (Sn=O), respectively.⁴⁸ The XPS results agree well with that of the XRD measurements. Both XRD and XPS characterizations indicate that SnO₂-SnO hybrid has been successfully fabricated through the hydrothermal process.

Fig. 2A and B shows the TEM images of the as-prepared pure SnO₂ nanoparticles at different magnifications. It can be seen that the obtained SnO₂ nanoparticles have tiny size. Due to the absence of any surfactants and supporting materials, the produced SnO₂ nanoparticles exhibit aggregates with porous structure. Meanwhile, the SnO₂-SnO hybrids obtained by using different tin precursors through the same hydrothermal process exhibit much

different morphology from that of pure SnO₂ material. Fig. 2C and D shows the TEM images of the SnO₂-SnO composite at different magnifications. It can be seen that in the composite, the

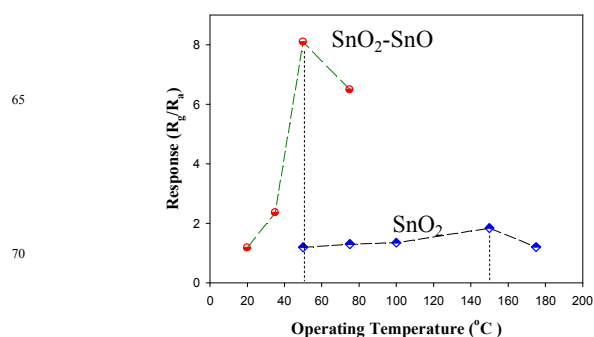


Fig. 4 Sensing responses of SnO₂-SnO and SnO₂ to 50 ppm NO₂ gas as a function of operating temperature.

SnO crystal exhibits laminal structure with several hundreds and tens nanometer in lateral size and thickness, respectively. At the same time, one layer of SnO₂ nanoparticles with approximately 4-10 nm in diameter are dispersed on the surface of the large SnO plates, forming the heterojunction structures. To further examine the p-n heterojunction structure, a typical HRTEM image of the SnO₂-SnO hybrid is shown in Fig. 2E. Highly crystalline SnO₂ nanocrystals with clear lattice fringes from different facets can be observed. Meanwhile, the lattice fringes corresponding to the (001) plane of SnO nanoplate can also be seen. The selected-area electron diffraction (SAED) pattern is shown in Fig. 2F. It can be seen that in addition to the diffraction cycles from multiple SnO₂ nanocrystals, there are also apparent diffraction spots, indicating the single crystalline phase of the SnO nanoplates. These electron microscopy analyses are in accordance with the above XRD and XPS measurements, showing the formation of SnO₂-SnO p-n structure with large SnO laminal crystals covered by small SnO₂ nanoparticles.

In order to quantitatively determine and compare the specific surface areas and pore volumes of the SnO₂ and SnO₂-SnO hybrids, multipoint BET surface area and pore volume measurements were carried out based on the nitrogen adsorption-desorption isotherms. The N₂ physisorption isotherms of the two samples and their corresponding Barret–Joyner–Halenda (BJH) pore size distribution curves are shown in Fig. 3. One can see that the SnO₂-SnO hybrids exhibit the isotherm feature of the H3 type according to the IUPAC classification, whereas the pure SnO₂ sample shows a H2 type. From the measurements, the BET surface areas of SnO₂-SnO and SnO₂ are 45.6 and 178.9 m²/g, respectively. As described above, the high surface area of the pure SnO₂ nanocrystals could be attributed to the small particle size and the porous structure which can be seen in the TEM characterization. On the basis of BJH model and the desorption data, the average pore radii $dV(d)$ of SnO₂-SnO composite and SnO₂ nanoparticles were calculated to be 1.68 and 4.3 nm, respectively, as shown in Fig. 3 insets.

3.2 Sensing performances of SnO₂-SnO hybrid and pure SnO₂ nanoparticles for NO₂ gas detection

The sensing performances of the SnO₂-SnO hybrid and single

Cite this: DOI: 10.1039/c0xx00000x

www.rsc.org/xxxxxx

ARTICLE TYPE

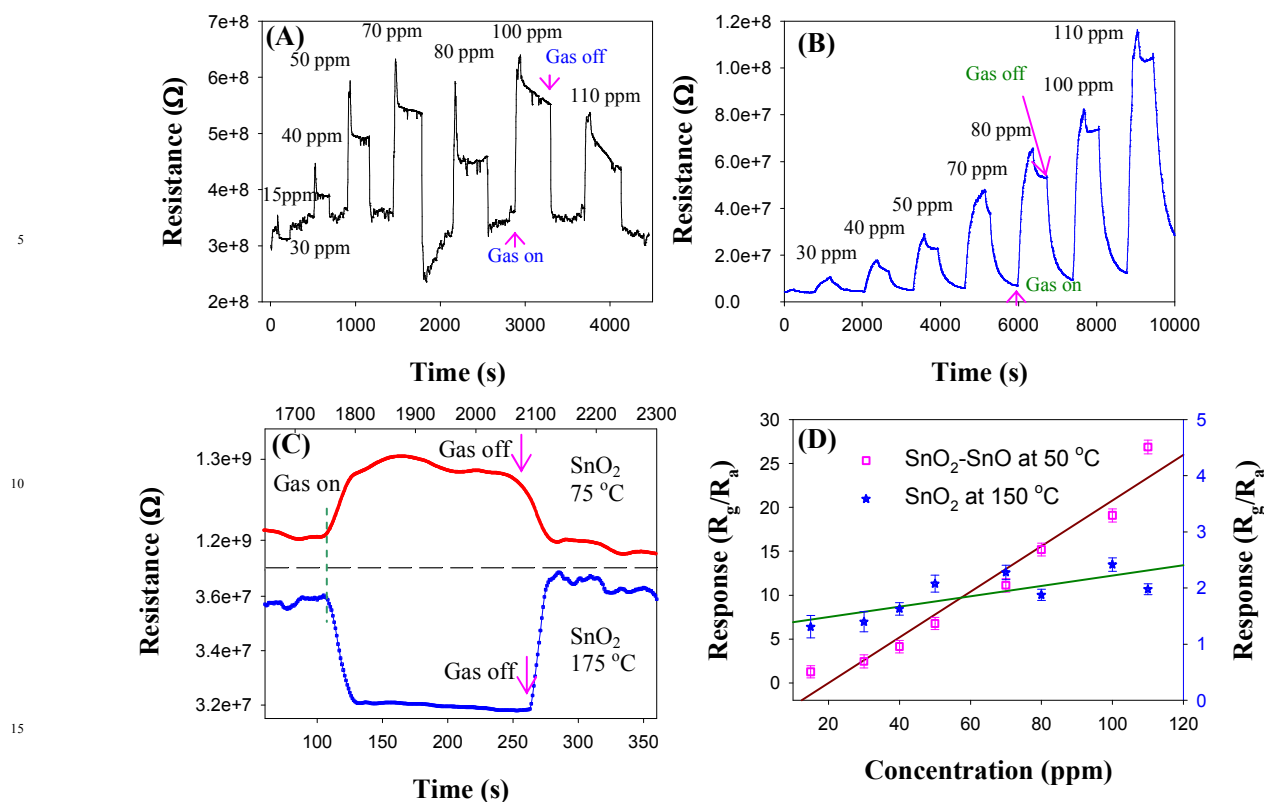


Fig. 5 Sensing responses of pure SnO₂ at 150 °C (A) and SnO₂-SnO at 50 °C (B) upon exposure to NO₂ gas with different concentrations varying from 15 to 110 ppm. (C) Sensing responses of pure SnO₂ to 50 ppm NO₂ gas at 75 °C (top) and 175 °C (bottom). (D) Response variations of SnO₂-SnO and SnO₂ as a function of NO₂ concentration at 50 and 150 °C, respectively. Solid lines show the linear fitting of the experimental data.

SnO₂ for NO₂ gas detection were studied and compared. First, operating temperature is one of important sensing properties of materials and low operating temperature is especially favorable for their practical application in real gas sensors. Fig. 4 shows the responses of the two materials towards 50 ppm NO₂ gas as a function of operating temperature. It can be seen that for both materials, the response intensity is dependent on the working temperature, i.e. increasing firstly with appearance of a peak, and then declining with the temperature further increasing. However, the response intensity and the optimum operating temperature are much different for the two materials. For the SnO₂-SnO hybrid, the sensing response gradually increases first with temperature increasing and reaches a maximum at 50 °C, and at even lower temperatures, ca. room temperature, the material still show weak response. Such result implies that after further optimization, sensors based on the SnO₂-SnO hybrids could have the sensing ability for NO₂ gas detection at room temperature. This is a big breakthrough for the semiconductor metal oxide-based gas sensor, since the NO₂ gas sensing can be achieved at room temperature without any aid of noble metal doping or large surface-area supports (e.g. graphene, carbon nanotubes).

However, the sensing response of the pure SnO₂ reaches the maximum at around 150 °C which is triple higher than that obtained from the SnO₂-SnO hybrid (50 °C). Moreover, the response intensity from pure SnO₂ is much lower than that of the SnO₂-SnO composite (about one fourth of the hybrid). From the XRD and TEM measurements, the particle size of pure SnO₂ is around 4 nm and the size of the SnO₂ nanoparticle on the surface of SnO is about 28 nm. According to the size effect, compared with larger nanoparticles, the smaller sized particles should have better sensing performance due to the larger surface area.⁴⁹ However, the present study showed that the SnO₂-SnO hybrid with larger particle size exhibited much higher sensing performance. Therefore, the enhanced sensing performance of the SnO₂-SnO hybrid should be ascribed to the unique p-n heterojunction structure. Such excellent gas sensing properties with enhanced sensing response and much lowered operating temperature make the novel SnO₂-SnO hybrid structure a kind of promising gas sensor material for NO₂ gas detection.

The dynamic sensing response and recovery properties of the pure SnO₂ and SnO₂-SnO for NO₂ detection were investigated. Fig. 5A and B shows the sensing responses of SnO₂ and SnO₂-

SnO as a function of concentration of NO₂ gas (from 15 to 110

Table 1 Summary of the gas sensing performances of SnO₂-based metal oxide nanomaterials with p-n heterostructure.

ppm) at 150 and 50 °C, respectively. From Fig. 5A, it can be seen that with the increase of NO₂ concentration, the resistance of the

Analyte gas	Composion	Synthesis route	Morphology	Opera. Temp. (°C)	Response (R _a -R ₀)/R ₀	Concentration	LOD	Ref.
NO ₂	WO ₃ -SnO ₂	Combinatorial solution deposition	SnO ₂ particles loaded on WO ₃ lamella		N/A	200 ppb	N/A	36
C ₂ H ₅ OH	ZnO-SnO ₂	Hydrothermal method	Core-shell		52.7	50 ppm	N/A	38
CH ₃ COCH ₃	Fe ₂ O ₃ -SnO ₂	Hydrothermal method	Core-shell		1.7	10 ppm	10 ppm	56
CH ₃ COCH ₃	Fe ₂ O ₃ -SnO ₂	Hydrothermal method	Fe ₂ O ₃ nanorods grew on SnO ₂ nanosheets		17	100 ppm	N/A	37
H ₂ S	CuO-SnO ₂	Chemical vapour deposition	CuO particles onto SnO ₂ nanowire	200		100 ppm	N/A	34
H ₂ S	CuO-SnO ₂	Electrospun	Composite nanowires	300	650	100 ppm	N/A	31
(CH ₃) ₂ CHOH	SnO ₂ -SnO ₂	Chemical precipitation	Mixed phase SnO ₂ nanorods	255	4.7	100 ppm	N/A	57
H ₂	SnO-SnO ₂	Hydrothermal method	SnO ₂ particles load on SnO nanorods	120	N/A	N/A	N/A	30
NO ₂	SnO-SnO ₂	Hydrothermal method	SnO ₂ nanoparticles loaded on SnO nanosheets	50	19.1	100 ppm	0.1 ppm	This work

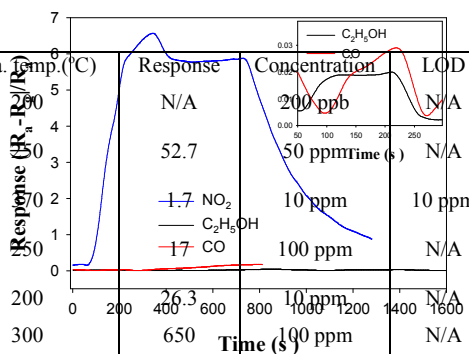


Fig. 6 Detection selectivity of the SnO₂-SnO for 100 ppm NO₂, C₂H₅OH and CO at 50 °C. Inset shows the magnified response cures for C₂H₅OH and CO.

pure SnO₂ exhibits a little change, indicating the non-sensitive of pure SnO₂ even if at high temperature (150 °C). However, as shown in Fig. 5B, at much lower temperature (50 °C), the resistance of the SnO₂-SnO hybrid shows increase with increasing NO₂ gas concentration. Moreover, the resistance can be almost completely recovered when the sensor was exposed to fresh air during the whole testing procedure. Such results indicate the high sensing sensitivity of the SnO₂-SnO hybrid toward NO₂ gas at low temperature and suggest that the sensing mechanism of the SnO₂-SnO composites corresponds to the typical n-type semiconductor metal oxides.

Interestingly, we also found that the pure SnO₂ exhibits different sensing characteristics at low and high temperatures. As shown in Fig. 5C, at 75 °C the introduction of 50 ppm NO₂ gas leads to the increase of the resistance of pure SnO₂. However, at 175 °C the presence of NO₂ gas can result in the decrease of the resistance of SnO₂, which is totally opposite to the behavior at low temperature. In other words, the pure SnO₂ exhibits n-type characteristics at low temperature (75 °C) but shows overturned sensing behavior at 175°C with p-type sensing mechanism, which is different from those reported previously.^{34, 45} We will discuss this issue in the following part of gas sensing mechanism. The responses of the SnO₂-SnO and pure SnO₂ as a function of NO₂ concentration are plotted in Fig. 5D. For the SnO₂-SnO hybrid in the whole concentration range, a good linear fit was obtained with R² = 0.943. From the slope of the calibration line, the sensitivity of the SnO₂-SnO hybrid for NO₂ detection was calculated to be 0.257 ppm⁻¹. Furthermore, the limit of detection (LOD) of the SnO₂-SnO was estimated to be 0.1 ppm based on the LOD = 3 α_D/α (where α is the slope of linear part of the calibration curve and α_D is the standard deviation of noise in the response curve in air).⁵⁰ In sharp contrast, a linear fit with R² = 0.555 was obtained from the pure SnO₂ nanoparticles. Compared with the high sensitivity and low LOD of the SnO₂-SnO, the pure SnO₂

material is not sensitive to the concentration variation of NO₂ gas (green fitting line) with the sensitivity and theoretical LOD of 0.007 ppm⁻¹ and 0.6 ppm, respectively. Meanwhile, it can be seen that the SnO₂ sensor reaches sensing saturation at very low concentration and thus the concentration change of the target gas can be hardly distinguished. These results strongly indicate that the SnO₂-SnO hybrid have enhanced sensing performance for NO₂ gas compared to pure SnO₂ nanomaterials. Table 1 summarizes the sensing performances of SnO₂-based hybrid metal oxide nanomaterials with p-n heterostructure for detection of different gases. Clearly, in this study, the optimum temperature, limit of detection and the response intensity to 100 ppm target gas almost exceed those in the previous reports. The sensing selectivity of the SnO₂-SnO hybrid for NO₂ gas was also examined. As shown in Fig. 6, with SnO₂-SnO exposed to 100 ppm NO₂, C₂H₅OH and CO at 50 °C, the response intensity to NO₂ is significantly larger than those to C₂H₅OH and CO gases, indicating the high selectivity of the p-n heterojunction nanostructure for NO₂ detection. The much enhanced sensing

performance of the SnO₂-SnO hybrid makes it promising sensing material in application of real NO₂ gas sensors.

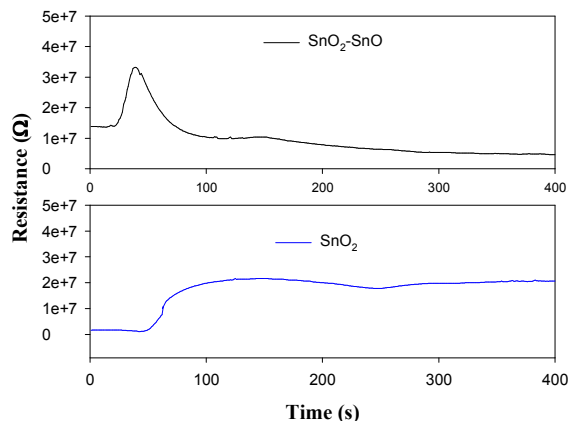


Fig. 7 Variation of resistance (R_a) measured in air with time for SnO₂-SnO (top) and SnO₂ (bottom) having varied temperature from approximately 20 to 200 °C (target temp.)

3.3 Gas sensing mechanism of the SnO₂-SnO composites with p-n heterojunction

From above studies, the SnO₂-SnO hybrid with p-n junction exhibited improved sensing properties compared to the pure SnO₂ material. Here, we propose a sensing mechanism of the SnO₂-SnO p-n heterojunction nanostructure. The semiconductive properties of the two materials were firstly studied.⁵¹ Fig. 7 shows the variation of resistances of hybrid SnO₂-SnO and pure SnO₂ materials in air as a function of time in the temperature range from ~20 to 200 °C. We can see that these two sensing materials show different variation tendency although they belong to the same type of semiconductor metal oxides (n-type). SnO₂ is a well known n-type semiconductor (majority carrier is electron). Thus, with temperature rising, the oxygen in air can be adsorbed on the surface of SnO₂ to create chemisorbed oxygen species (O₂⁻, O⁻, O₂²⁻) and consume the inner electrons. Such process could produce surface polarization energy level and result in the increase of bulk resistance. With oxygen species concentration reach saturation, bulk resistance entry a relative stable state (bottom of Fig. 7). As shown in top of Fig. 7, the resistance variation of SnO₂-SnO is a little more complicated than the pure SnO₂ sample. Compared with n-type SnO₂, SnO belongs to p-type semiconductor (majority carrier is hole).^{30, 52} With temperature increasing, the resistance of the hybrid rises firstly and then declines to a stable state, which can be explained as follows. In the composite, oxygen is firstly adsorbed on the surface of the SnO₂ material and the oxygen ionization process can consume large amount of free electrons and thus holes were left in the composites, leading to the increase of resistance just like the pure SnO₂. With temperature further increasing, SnO nanocrystals become the active and main component for chemisorption of oxygen, resulting in the further increase of holes concentration in the conduction band of the composite. The increase of holes concentration can enhance the speed of electron penetration on both sides of p-n heterojunction, resulting in the declining tendency of the resistance of the hybrids. Similar to the pure

SnO₂ sample, the resistance reaches a relative stable value in the end.

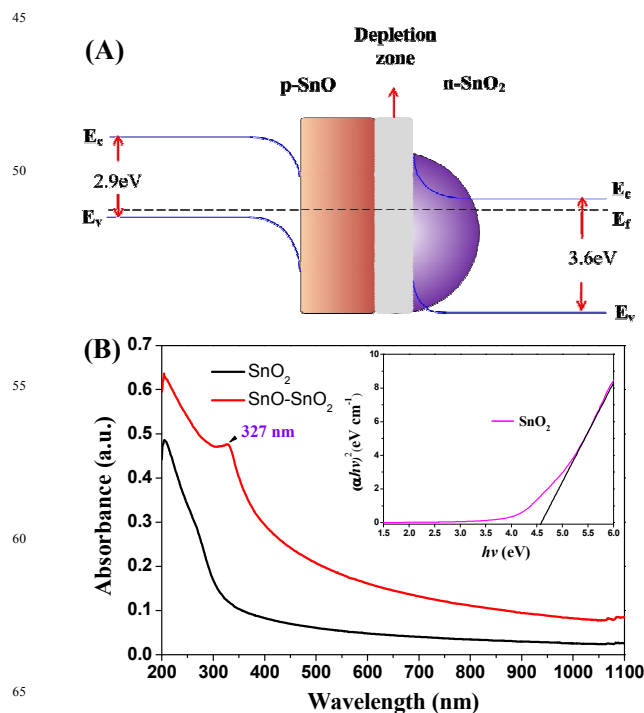


Fig. 8 (A) General schematic of the heterostructure of n-SnO₂ nanoparticles on the surface of p-SnO nanosheets with a p-n junction. (B) UV-vis spectra of SnO₂-SnO and pure SnO₂ materials. Inset shows the plot of $(ahv)^2$ versus (hv) from the pure SnO₂.

The n-type SnO₂ and p-type SnO can form a heterojunction structure at the interface, which is considered to be the primary reason for the enhanced sensing response and low operation temperature of the hybrid material.⁵³ As shown in Fig. 8A, theoretically the forbidden band width between E_c (conduction band) and E_v (valence band) is 3.6 eV in SnO₂ semiconductor and is about 2.9 eV in SnO. The p-n heterojunction leads to the formation of depletion region. It can be seen that the bending of forbidden bands occurs at the interface zone to make the E_f (Fermi level) equilibrium between SnO₂/SnO band gaps. In general, the narrower the width of forbidden band, the lower energy is required for the transition of electrons near the bottom of the conduction band. The UV-vis spectra of the SnO₂-SnO and pure SnO₂ materials are shown in Fig. 8B, from which the band gaps of these two samples can be evaluated. From the calculations, even though the actual forbidden band widths of these two samples are larger than that of bulk SnO₂ (3.6 eV) due to the quantum confinement effect, the band width of the SnO₂-SnO hybrid is much lower (3.79 eV) than that of pure SnO₂ (4.6 eV). The change of the band gap can well explain the reason that the operation temperature of the SnO₂-SnO composites is much lower than that of the pure n-SnO₂. Meanwhile, as soon as the concentration of the oxygen anions (mainly O⁻) gets a saturation value, the height of potential barrier and the width of depletion region will not change.⁵⁴ The width of depletion zone will directly decide the response of a sensor at low temperature ranges. When the sensors are exposed to NO₂ gas (oxidizing gas),

NO₂ molecules are absorbed on the surface of both SnO₂ and uncovered SnO. Similar to the pure SnO₂ sensor, the absorbed NO₂ can capture the electrons from the conduction bands of the semiconductors, resulting in the increase of the resistance of SnO₂-SnO composites which can be seen in Fig. 5B. After trapping electrons from conduction band and anion oxygen, NO₂ gas molecules became NO₂⁻. At the same time, chemisorbed oxygen species were released to air once more. When the surface of samples are almost fully covered by NO₂⁻, the mobility of free electrons on the surface are largely reduced and make the resistance of composites increase to a saturation value. Meanwhile, the reduced mobility of free electrons and the increased holes concentration could lead to the increase of thickness of depletion region, which may be another reason for the increase of sensor resistance.⁴⁷

When NO₂ was adsorbed on pure SnO₂, owing to the strong oxidability of NO₂, the electrons captured by NO₂ can be hardly exchanged with fresh oxygen, which may be responsible for the poor recovery of pure SnO₂. On the other hand, when the pure SnO₂ sensor was exposed to NO₂ gas at high temperature, because of the hard releasing of captured electron, NO₃⁻ can be formed on the surface of composites, and meanwhile, abundant holes are left in the conduction band and become the major carriers. Therefore, the SnO₂ showed p-type semiconductor properties and the resistance showed a decrease in the process. Such interesting phenomenon (called percolation behavior) has also been reported by Neri et al.^{51, 55}

4. Conclusion

The gas sensing properties of SnO₂-SnO composite material with p-n heterojunction structure have been investigated for detection of NO₂ gas. The results showed that the sensing performance of the SnO₂-SnO hybrid is much higher than that of pure SnO₂ nanoparticles. The optimum temperature of SnO₂-SnO sensor is as low as 50 °C, at which the sensor showed excellent linearity between sensing response and the concentration of NO₂ gas with a wide concentration range (15 to 110 ppm), low LOD (ca. 0.1 ppm) and good selectivity. Even though the pure SnO₂ nanoparticles possess small crystalline grain size and large specific surface area, the sensing performance of pure SnO₂ for NO₂ gas detection is still lower than that of the SnO₂-SnO hybrids. In the proposed sensing mechanism, the p-n heterojunction structure formed at the interface of SnO₂-SnO may account for the improved sensing performance, especially the much lowered operation temperature. The present study shows that in addition to optimizing crystal size and improving specific surface area, fabricating semiconductor materials with p-n heterojunction structure is also a very efficient way to design gas sensor with high sensing performance.

Acknowledgements

This work was supported by the National Natural Science Foundation of China (No. 21275136), the Natural Science Foundation of Jilin province, China (No. 201215090) and Jilin province postdoctoral scientific research project (No. RB201317).

Notes and references

- ^a State Key Laboratory of Electroanalytical Chemistry, Changchun Institute of Applied Chemistry, Chinese Academy of Sciences, Changchun 130022, Jilin, People's Republic of China. Tel: +86431-85262723; E-mail: weichen@ciac.ac.cn
- ^b The College of Electrical and Electronic Engineering, Changchun University of Technology, Changchun 130012, People's Republic of China
- ^c University of Chinese Academy of Sciences, Beijing 100039, People's Republic of China
- † Electronic Supplementary Information (ESI) available: Survey XPS spectrum of the SnO₂-SnO hybrid material. See DOI: 10.1039/b000000x/
- H. K. Wang and A. L. Rogach, *Chem. Mater.*, 2014, **26**, 123-133.
- Z. W. Chen, D. Y. Pan, Z. Li, Z. Jiao, M. H. Wu, C. H. Shek, C. M. L. Wu and J. K. L. Lai, *Chem. Rev.*, 2014, **114**, 7442-7486.
- M. D'Arienzo, D. Cristofori, R. Scotti and F. Morazzoni, *Chem. Mater.*, 2013, **25**, 3675-3686.
- T. Kida, S. Fujiyama, K. Suematsu, M. Yuasa and K. Shimanoe, *J. Phys. Chem. C*, 2013, **117**, 17574-17582.
- K. Suematsu, Y. Shin, Z. Q. Hua, K. Yoshida, M. Yuasa, T. Kida and K. Shimanoe, *ACS Appl. Mater. Inter.*, 2014, **6**, 5319-5326.
- X. L. Wang, N. Aroonyadet, Y. Z. Zhang, M. Meckenburg, X. Fang, H. T. Chen, E. Goo and C. W. Zhou, *Nano Lett.*, 2014, **14**, 3014-3022.
- N. D. Chinh, N. V. Toan, V. V. Quang, N. V. Duy, N. D. Hoa and N. V. Hieu, *Sensor Actuat. B-Chem.*, 2014, **201**, 7-12.
- Y. J. Chen, L. Nie, X. Y. Xue, Y. G. Wang and T. H. Wang, *Appl. Phys. Lett.*, 2006, **88**, 083105.
- Y. J. Chen, X. Y. Xue, Y. G. Wang and T. H. Wang, *Appl. Phys. Lett.*, 2005, **87**, 233503.
- Z. Lou, L. L. Wang, R. Wang, T. Fei and T. Zhang, *Solid State Electron.*, 2012, **76**, 91-94.
- Y. Liu, Y. Jiao, Z. Zhang, F. Qu, A. Umar and X. Wu, *ACS Applied Materials & Interfaces*, 2014, **6**, 2174-2184.
- L. W. Wang, S. R. Wang, Y. S. Wang, H. X. Zhang, Y. F. Kang and W. P. Huang, *Sensor Actuat. B-Chem.*, 2013, **188**, 85-93.
- L. Mei, J. W. Deng, X. M. Yin, M. Zhang, Q. H. Li, E. D. Zhang, Z. Xu, L. B. Chen and T. H. Wang, *Sensor Actuat. B-Chem.*, 2012, **166**, 7-11.
- C. P. Gu, X. J. Xu, J. R. Huang, W. Z. Wang, Y. F. Sun and J. H. Liu, *Sensor Actuat. B-Chem.*, 2012, **174**, 31-38.
- A. V. Tadeev, G. Delabouglise and M. Labeau, *Thin Solid Films*, 1999, **337**, 163-165.
- P. Ivanov, E. Llobet, X. Vilanova, J. Brezmes, J. Hubalek and X. Correig, *Sensor Actuat. B-Chem.*, 2004, **99**, 201-206.
- G. Neri, A. Bonavita, G. Micali, N. Donato, F. A. Deorsola, P. Mossino, I. Amato and B. De Benedetti, *Sensor Actuat. B-Chem.*, 2006, **117**, 196-204.
- X. Y. Xue, Z. H. Chen, C. H. Ma, L. L. Xing, Y. J. Chen, Y. G. Wang and T. H. Wang, *J. Phys. Chem. C*, 2010, **114**, 3968-3972.
- Y. C. Lee, H. Huang, O. K. Tan and M. S. Tse, *Sensor Actuat. B-Chem.*, 2008, **132**, 239-242.
- Z. Zhang, L. Liu, Q. Qi, S. C. Li and G. Y. Lu, *Sensor Actuat. B-Chem.*, 2009, **139**, 287-291.
- P. Sun, Y. S. Yu, J. Xu, Y. F. Sun, J. Ma and G. Y. Lu, *Sensor Actuat. B-Chem.*, 2011, **160**, 244-250.
- B. Kim, Y. J. Lu, A. Hannon, M. Meyyappan and J. Li, *Sensor Actuat. B-Chem.*, 2013, **177**, 770-775.
- C. Jin, H. Kim, S. Park, H. W. Kim, S. Lee and C. Lee, *Ceram. Int.*, 2012, **38**, 6585-6590.
- F.-C. Chung, R.-J. Wu and F.-C. Cheng, *Sensors and Actuators B: Chem.*, 2014, **190**, 1-7.
- J. Zhang, X. H. Liu, S. H. Wu, M. J. Xu, X. Z. Guo and S. R. Wang, *J. Mater. Chem.*, 2010, **20**, 6453-6459.
- S. W. Choi, A. Katoch, G. J. Sun, P. Wu and S. S. Kim, *J. Mater. Chem. C*, 2013, **1**, 2834-2841.
- R.-J. Wu, D.-J. Lin, M.-R. Yu, M. H. Chen and H.-F. Lai, *Sensors and Actuators B: Chemical*, 2013, **178**, 185-191.
- M. M. Liu, R. Z. Zhang and W. Chen, *Chem. Rev.*, 2014, **114**, 5117-5160.

29. F. F. Ren, C. Q. Wang, C. Y. Zhai, F. X. Jiang, R. R. Yue, Y. K. Du, P. Yang and J. K. Xu, *J. Mater. Chem. A*, 2013, **1**, 7255-7261.
30. A. Shanmugasundaram, P. Basak, L. Satyanarayana and S. V. Manorama, *Sensor Actuat. B-Chem.*, 2013, **185**, 265-273.
31. S. W. Choi, A. Katoch, J. Zhang and S. S. Kim, *Sensor Actuat. B-Chem.*, 2013, **176**, 585-591.
32. M. Mashock, K. H. Yu, S. M. Cui, S. Mao, G. H. Lu and J. H. Chen, *ACS Appl. Mater. Inter.*, 2012, **4**, 4192-4199.
33. N. D. Khoang, D. D. Trung, N. V. Duy, N. D. Hoa and N. V. Hieu, *Sensor Actuat. B-Chem.*, 2012, **174**, 594-601.
34. F. Shao, M. W. G. Hoffmann, J. D. Prades, R. Zamani, J. Arbiol, J. R. Morante, E. Varechkina, M. Rumyantseva, A. Gaskov, I. Giebelhaus, T. Fischer, S. Mathur and F. Hernandez-Ramirez, *Sensor Actuat. B-Chem.*, 2013, **181**, 130-135.
35. Z. J. Wang, Z. Y. Li, J. H. Sun, H. N. Zhang, W. Wang, W. Zheng and C. Wang, *J. Phys. Chem. C*, 2010, **114**, 6100-6105.
36. T. Kida, A. Nishiyama, Z. Hua, K. Suematsu, M. Yuasa and K. Shimano, *Langmuir*, 2014, **30**, 2571-2579.
37. P. Sun, Y. X. Cai, S. S. Du, X. M. Xu, L. You, J. Ma, F. M. Liu, X. S. Liang, Y. F. Sun and G. Y. Lu, *Sensor Actuat. B-Chem.*, 2013, **182**, 336-343.
38. W. W. Guo, T. M. Liu, R. Sun, Y. Chen, W. Zeng and Z. C. Wang, *Mater. Lett.*, 2012, **89**, 5-8.
39. G. W. She, X. Huang, L. L. Jin, X. P. Qi, L. X. Mu and W. S. Shi, *Small*, 2014, **10**, 4685-4692.
40. K. T. Lee, C. H. Lin and S. Y. Lu, *J. Phys. Chem. C*, 2014, **118**, 14457-14463.
41. Y. Chen, J. Lu, S. Wen, L. Lu and J. M. Xue, *J. Mater. Chem. A*, 2014, **2**, 17857-17866.
42. S. H. Ahn, D. J. Kim, W. S. Chi and J. H. Kim, *Adv. Funct. Mater.*, 2014, **24**, 5037-5044.
43. L. Li, S. J. He, M. M. Liu, C. M. Zhang and W. Chen, *Anal. Chem.*, 2015, **87**, 1638-1645.
44. H. Zhang, J. C. Feng, T. Fei, S. Liu and T. Zhang, *Sensor Actuat. B-Chem.*, 2014, **190**, 472-478.
45. A. Sharma, M. Tomar and V. Gupta, *Sensor Actuat. B-Chem.*, 2013, **176**, 875-883.
46. H. J. Song, L. C. Zhang, C. L. He, Y. Qu, Y. F. Tian and Y. Lv, *J. Mater. Chem.*, 2011, **21**, 5972-5977.
47. F. Song, H. L. Su, J. J. Chen, W. J. Moon, W. M. Lau and D. Zhang, *J. Mater. Chem.*, 2012, **22**, 1121-1126.
48. H. L. Huang, Y. J. Liu, Q. Z. Gao, W. S. Ruan, X. M. Lin and X. Li, *ACS Appl. Mater. Inter.*, 2014, **6**, 10258-10264.
49. C. N. Xu, J. Tamaki, N. Miura and N. Yamazoe, *Sensor Actuat. B-Chem.*, 1991, **3**, 147-155.
50. R. K. Paul, S. Badhulika, N. M. Saucedo and A. Mulchandani, *Anal. Chem.*, 2012, **84**, 8171-8178.
51. G. Neri, S. G. Leonardi, M. Latino, N. Donato, S. Baek, D. E. Conte, P. A. Russo and N. Pinna, *Sensor Actuat. B-Chem.*, 2013, **179**, 61-68.
52. A. K. Sinha, P. K. Manna, M. Pradhan, C. Mondal, S. M. Yusuf and T. Pal, *Rsc Adv.*, 2014, **4**, 208-211.
53. X. H. Zhou, Q. X. Cao, H. Huang, P. Yang and Y. Hu, *Mater. Sci. Eng. B-Adv.*, 2003, **99**, 44-47.
54. L. I. Trakhtenberg, G. N. Gerasimov, V. F. Gromov, T. V. Belysheva and O. J. Ilegbusi, *Sensor Actuat. B-Chem.*, 2012, **169**, 32-38.
55. N. Savage, B. Chwieroth, A. Ginwalla, B. R. Patton, S. A. Akbar and P. K. Dutta, *Sensor Actuat. B-Chem.*, 2001, **79**, 17-27.
56. S. F. Zhang, F. Ren, W. Wu, J. Zhou, X. H. Xiao, L. L. Sun, Y. Liu and C. Z. Jiang, *Phys. Chem. Chem. Phys.*, 2013, **15**, 8228-8236.
57. D. Hu, B. Q. Han, S. J. Deng, Z. P. Feng, Y. Wang, J. Popovic, M. Nuskol, Y. D. Wang and I. Djerdj, *J. Phys. Chem. C*, 2014, **118**, 9832-9840.